International Journal of Remote Sensing

ISSN: 0143-1161 (Print) 1366-5901 (Online) Journal homepage: www.tandfonline.com/journals/tres20

Non-redundant Golay formations for high-resolution L-band aperture synthesis

Matas Gelžinis & Alexander Wittig

To cite this article: Matas Gelžinis & Alexander Wittig (18 Dec 2025): Non-redundant Golay formations for high-resolution L-band aperture synthesis, International Journal of Remote Sensing, DOI: 10.1080/01431161.2025.2603694

To link to this article: https://doi.org/10.1080/01431161.2025.2603694

Published online: 18 Dec 2025.

INTERNATIONAL JOURNAL OF REMOTE SENSING
https://doi.org/10.1080/01431161.2025.2603694

Taylor & Francis
Taylor & Francis Group

Non-redundant Golay formations for high-resolution L-band aperture synthesis

Matas Gelžinis and Alexander Wittig

Department of Aeronautics and Astronautics, University of Southampton, Southampton, UK

ABSTRACT

This study explores various satellite formations for passive microwave interferometry, aimed at sensing soil moisture and ocean salinity in the L-band. Golay-based satellite formations offer the largest *uv* coverage for a given number of satellites by minimising redundancy in inter-satellite baselines, which makes them especially well-suited for this purpose. We demonstrate that distributing the same total number of antennas as in the TriHex mission concept (Golay3) across nine smaller satellites (Golay9) yields an improved angular resolution of 1.36° and a reduced maximum sidelobe level of −14.39 dB. Applying the Golay9 formation to the HexSat nanosatellite platform could yield L-band ground resolutions of less than 6 km from an altitude of 250 km.

ARTICLE HISTORY
Received 4 September 2025
Accepted 1 December 2025

KEYWORDS
Golay formations; non-redundant 2D interferometer arrays; synthetic aperture radiometry; HexSats

1. Introduction

Surface soil moisture and sea surface salinity are critical variables in hydrology, forming a vital link between the Earth's surface and the atmosphere. They influence key processes such as evaporation, precipitation and runoff (Berger et al. 2002) and play important roles in flood forecasting and drought monitoring (Beljaars et al. 1996; Dirmeyer and Brubaker 1999). Soil moisture affects agricultural productivity (Nairizi and Rydzewski 1977), while ocean salinity drives large-scale weather patterns and climate variability (Lukas and Lindstrom 1991).

Microwave radiometry has emerged as an effective method for observing these variables from space. The emitted microwave radiation from soil or water depends primarily on its dielectric constant, which is strongly influenced by soil moisture (Schmugge 1980) and, to a lesser extent, by salinity (Lang et al. 2016). Low-frequency microwave bands are preferred because they penetrate deeper into the soil and are less affected by surface roughness and water temperature variations (Johnson et al. 2021). The lowest protected frequency band for passive remote sensing is the L-band (1.4–1.427 GHz), which provides the best available penetration and sensitivity.

At L-band, diffraction limits spatial resolution and drives the need for large apertures (Condon and Ransom 2016). Real-aperture missions illustrate this trade-off: SMAP's 6 m

CONTACT Matas Gelžinis mg2n18@soton.ac.uk Department of Aeronautics and Astronautics, University of Southampton, University Road, Southampton SO17 1BJ, UK

This article has been corrected with minor changes. These changes do not impact the academic content of the article.

reflector delivers a roughly 40 km resolution, whereas CIMR's larger 8.5 m dish but higher orbit yields 60 km ground resolution at L-band (Entekhabi et al. 2010; European Space Agency 2024; Jiménez et al. 2021). Aperture synthesis mitigates this by emulating a large aperture with many small antennas; SMOS demonstrated the approach with 72 elements on three 4.5 m arms, achieving sub-50 km resolution (Kerr et al. 2001; Le Vine et al. 1994).

Despite this progress, SMOS resolution remains too coarse for many applications. Kerr et al. (2019) and Kerr et al. (2020) found that the spatial resolution should be at least 10 km to satisfy most L-band applications like carbon cycle monitoring, fire risk assessment or ice sheet temperature profiling. Prior work has identified three-satellite formations to improve resolution (Akins et al. 2025; Goutoule and De Boer 2000; Martín-Neira et al. 2023). In this work, we extend this concept by investigating formations composed of a larger number of smaller satellites. This comes at the cost of implementation challenges, some of which we discuss in Section 6. We continue the work presented in (Gelzinis and Wittig 2025) and demonstrate that Golay formations can maximise interferometric *uv* coverage for a given number of satellites by minimising redundancy. This leads to improved point spread characteristics, specifically in terms of half-power beamwidth and sidelobe suppression.

2. Background

Synthetic aperture radiometers recover the scene's brightness temperature by sampling its two-dimensional Fourier transform across spatial frequencies set by the instrument geometry (Ruf et al. 1988; Ulaby, Moore, and Fung 1981). The measured quantity – the visibility function $\mathcal{V}(u,v)$—is related to the brightness distribution $T_B(\xi,\eta)$ by (Corbella et al. 2004)

$$\mathcal{V}(u,v) = \iint\limits_{\xi^2+\eta^2\leq 1} T_B(\xi,\eta)\, e^{-2\pi j(u\xi+v\eta)} d\xi\, d\eta. \tag{1}$$

Here (u,v) are spatial frequencies in a plane perpendicular to boresight, and (ξ,η) are direction cosines describing the angular position of the source. Since the quantity of interest is brightness temperature, Equation 1 is inverted as

$$T_B(\xi,\eta) = \int\limits_{-\infty}^{\infty}\!\!\int \mathcal{V}(u,v) e^{2\pi j(u\xi+v\eta)} du\, dv. \tag{2}$$

In practice, $\mathcal{V}$ corresponds to a modified brightness temperature $\widetilde{T}_B(\xi,\eta)$ which takes into account the antenna's solid angle, normalised pattern and physical temperature (Moreno-Galbis, Kainulainen, and Martin-Neira 2007). To isolate and evaluate formation geometry effects on imaging performance, we adopt the best-case assumption $\widetilde{T}_B \approx T_B$.

Visibilities are sampled by cross-correlating signals from antenna pairs; each pair defines a baseline $\boldsymbol{b} = (u,v)$—the antenna separation projected onto the *uv* plane and normalised by the centre wavelength λ_0—yielding one spatial-frequency sample (Christensen et al. 2007). The antenna layout sets the baseline distribution: regular grids produce regular *uv* lattices that permit approximating the integral of Equation 2 with a

discrete Fourier sum, enabling the use of established fast Fourier transform methods (Camps et al. 1997). Alternative strategies can also shape the baseline grid: Sugihara El Maghraby et al. (2018) showed that rotating one array yields much larger, denser *uv* coverage with fewer antennas, and non-uniform layouts (Camps et al. 2008) can likewise expand coverage. These strategies are compatible with the formations considered here; however, for performance comparisons, we adopt a best-case assumption of a constant and uniform *uv* grid.

Among the possible grid layouts, hexagonal arrangements are often favoured due to their hardware efficiency and reduced element count compared to square grids (Sharp 1961). An example of this is the Y shape, used in the SMOS mission. One drawback of a Y-shaped arrangement, however, is that most *uv* points are non-redundant, making the system vulnerable to single-point failures. An alternative was proposed in the SMOS follow-on mission (Zurita et al. 2013), to arrange antennas along the perimeter of a hexagon. This results in a densely filled hexagonal *uv* sampling grid, with most points exhibiting double redundancy. Furthermore, arranging antennas in a hexagonal outline is advantageous when multiple arrays operate in formation. If neighbouring arrays are positioned the right distance apart, their individual *uv* hexagons tile well, resulting in an unbroken hexagonal grid.

3. Interferometric formations

One example of multiple interferometer arrays flying in a formation is the TriHex mission concept (Martín-Neira et al. 2023). A simplified version of TriHex is shown in Figure 1(a), with 36 antennas per satellite instead of 72 to make the concept clearer. The resulting *uv* cover is shown in Figure 1(b) with the colour of each point indicating which satellite pair produced it. Intra-satellite baselines produce the centre grey tile, which is repeated three times, once for each satellite.

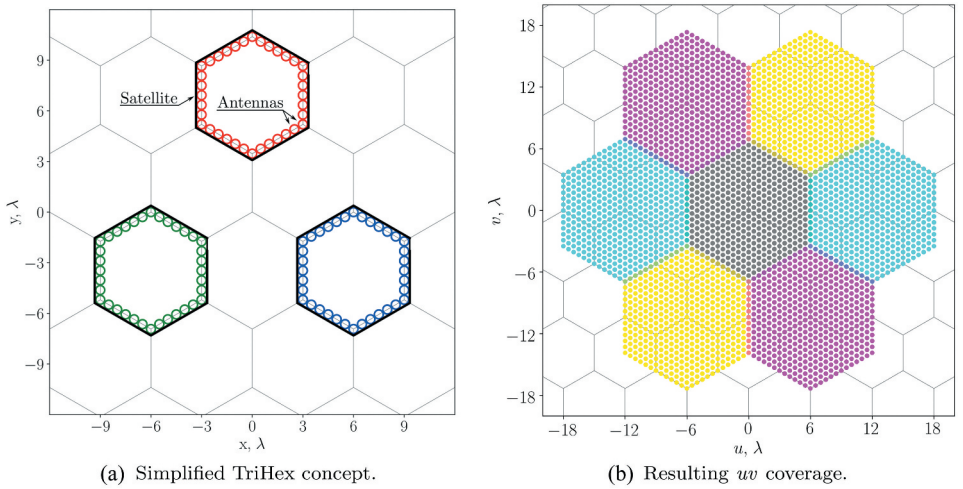

(a) Simplified TriHex concept. (b) Resulting *uv* coverage.

Figure 1. TriHex-like layout, but with 36 antennas per satellite (*a*) and the resulting *uv* coverage (*b*).

It is evident that TriHex adopts two separate configurations for arranging its antennas and satellites. We will refer to these as levels, with level 1 being the antenna arrangements on individual satellites and level 2 being the satellite arrangement in a formation. The idea of applying structured array patterns at multiple hierarchical levels can be naturally extended beyond just individual satellites and formations. As noted by McKay, Grydeland, and Gustavsson (2022), this concept allows for further scaling. For example, level 3 could govern the positioning of clusters of formations, while level 4 could describe the arrangement of a full constellation of clusters. In this work, however, we limit our analysis to levels 1 and 2 only, as they are the most relevant to current formation-flying architectures.

The satellites in Figure 1(a) are spaced so that their *uv* tiles have exactly one row of overlapping points. This is achieved when the distance between the closest antennas on neighbouring satellites is the same as the distance between the closest antennas on opposite edges of the same satellite. Specifically, the distance r between satellite centres is set to four times the inradius of the hexagon along whose perimeter the antennas are arranged:

$$r = 4N_\mathrm{a}s_\mathrm{a}\cos 30^\circ = 4N_\mathrm{a}s_\mathrm{a}\frac{\sqrt{3}}{2}, \tag{3}$$

where N_a is the number of antennas along each hexagon edge and s_a is the inter-antenna spacing. The term $N_\mathrm{a}s_\mathrm{a}$ then gives the distance from a satellite's centre to the centre of a corner antenna. Under anti-aliasing conditions, where $s_\mathrm{a} = \lambda/\sqrt{3}$ (Martín-Neira et al. 2023), the inter-satellite distance simplifies to

$$r = 2N_\mathrm{a}\lambda. \tag{4}$$

Note that the required satellite spacing depends on both the number of antennas per satellite and the observing wavelength. Smaller satellites – with fewer antennas – must be placed closer together to form the medium-length baselines that are absent within each satellite. Similarly, shorter wavelengths require tighter formations to maintain the same *uv* grid. This highlights why multi-satellite formations are not useful for short wavelengths: at higher frequencies, such as Ka-band (36.5 GHz), the necessary inter-satellite spacing drops below 20 cm for a satellite with 12 antennas per side. In that case, single-satellite solutions are more feasible.

This demonstrates that a hexagonal layout for the level 1 arrangement offers several advantages. However, the appropriate configuration for the level 2 satellite arrangement in formations with more than three satellites remains to be determined. Conceptually, this challenge is analogous to the problem of antenna placement: it involves balancing redundancy and coverage. In this context, we assume that the level 1 (intra-satellite) hexagonal layout provides sufficient baseline redundancy, with most *uv* points sampled at least twice, as in Martín-Neira et al. (2023). The focus then shifts to the level 2 (inter-satellite) configurations, where the goal is to minimise redundancy by ensuring that each inter-satellite baseline is unique, while maintaining minimal gaps. This maximises the number of distinct *uv* samples obtainable from a fixed number of satellites, without increasing sidelobes.

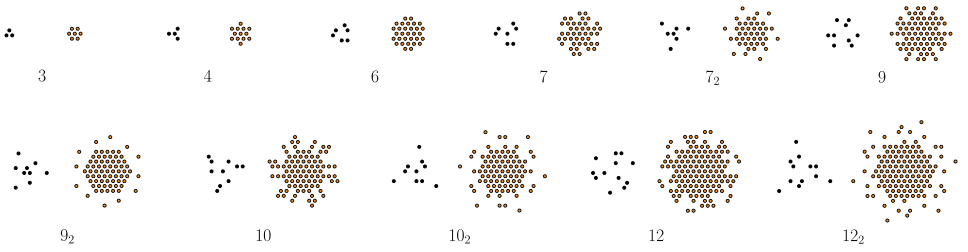

Figure 2. Threefold symmetric arrays on a hexagonal grid (black) with the most compact *uv* coverage (orange) presented by Golay (1971). Subscript '2' signifies an array with the largest core.

4. Golay arrays

The design of non-redundant satellite formations can be guided by the compact, threefold symmetric Golay point arrays introduced by Golay (1971). Shown in Figure 2, these are 2D point arrays with non-repeating relative spacings for up to 12 points. Each Golay array is denoted by its number of points (e.g. Golay9), and where applicable, Golay also proposed variants with the largest central core – defined as the configurations with baselines that fill the largest possible circle centred at the *uv* origin, including all interior points and half the points lying on the boundary. The largest core arrays are labelled in this work with a subscript '2'.

Golay used an algorithm to find n-point arrays with two important qualities: their spacings are non-redundant, which means that each baseline is unique, and they are compact, meaning that *uv* gaps are minimised. Other non-redundant 2D designs exist. Costas arrays (Golomb and Taylor 1984), originally developed for sonar applications, lie on rectangular grids and thus forfeit the hexagonal-grid advantages noted in Section 2. The Manx array (McKay, Grydeland, and Gustavsson 2022) reidentifies the Golay6 configuration. Honeycomb arrays (Blackburn et al. 2009) exhibit substantial *uv* gaps and, in some cases (e.g. radii 10 and 13), even include redundant baselines. Despite the merits of Golay layouts, notice from Figure 2 that *uv* gaps start to appear for arrays with more than six points. That is an unavoidable consequence of increasing the number of points in an array while sticking to the non-redundant spacing condition.

It is possible to choose any arrangement for levels 1 and 2. However, given the advantages outlined in Section 3, a hexagonal perimeter layout is selected for the level 1 antenna arrangement. Golay point arrays are subsequently adopted for the level 2 satellite configuration. This combination is beneficial because the resulting *uv* layout falls on a regular hexagonal grid, tiles well and has comparably few high redundancy (4+) baselines. An example of this combination is shown in Figure 3(a) with six hexagonal satellites in a Golay6 formation. Their baselines, with colour indicating redundancy, are shown in Figure 3(b). Most baselines are doubly redundant, a result of the symmetric antenna layout on each satellite. The central *uv* tile has an unavoidably high redundancy, since each satellite has an identical internal structure. However, non-central *uv* tiles, which result from inter-satellite baselines, do not overlap when using Golay formations. This maximizes the number of unique measurements for a given number of satellites.

Notice that the Golay3 level 2 arrangement is exactly the case used by TriHex (Martín-Neira et al. 2023) and shown in Figure 1. The TriHex paper also briefly references

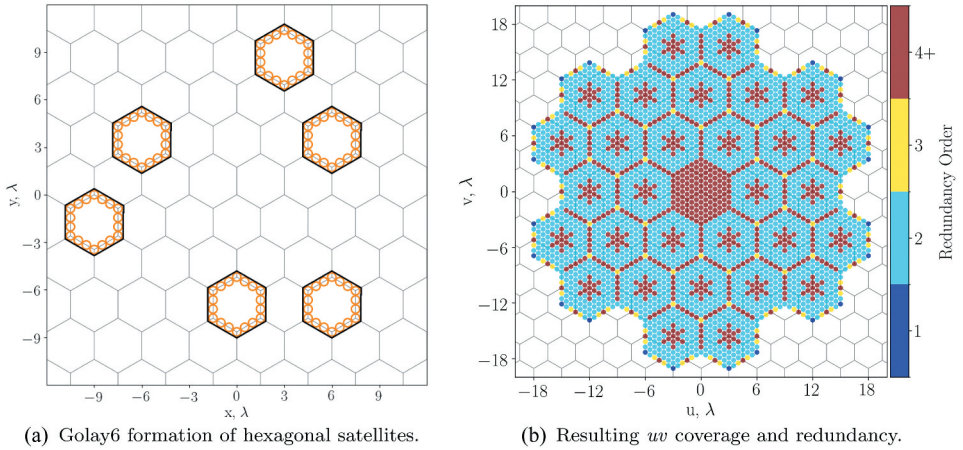

(a) Golay6 formation of hexagonal satellites. (b) Resulting *uv* coverage and redundancy.

Figure 3. Golay6 formation (*a*) and its resulting *uv* coverage, with baseline redundancy (*b*).

the 'FFLAS-2 Lite-6' formation, which corresponds to the Golay4 array used at level 2. In the following section, we compare several other Golay-based satellite formations to evaluate their performance in terms of their L-band synthetic beam sidelobe levels and 3 dB beamwidth.

5. Formation performance

Figure 4 compares the performance of several Golay-based satellite formations, each containing a total of 216 antennas. The only variable is the spatial distribution of the antennas. As the number of satellites increases, the size of each individual satellite decreases to maintain a constant overall antenna count. The first formation in Figure 4, Golay3, is identical to the TriHex mission concept proposed by Martín-Neira et al. (2023), where each of the three hexagonal satellites is 3 metres in diameter and contains 72 antennas.

In addition to showing satellite layouts and baseline distributions, Figure 4 presents the resulting Array Factor (AF), also referred to as the synthetic beam or the point response. It shows how well the available baselines recover a point source. The visibility function is then given by Equation 1, with a Dirac delta function used as the input brightness temperature map T_B. The recovered map is computed by approximating Equation 2 as a discrete sum (Akins et al. 2025; Ruf et al. 1988) over the N measurements $\mathcal{V}_i$ at each unique baseline (u_i, v_i)

$$AF(\xi,\eta) = \sum_{i=0}^{N-1} \mathcal{V}_i(u_i, v_i) W_i e^{2\pi j(u_i\xi + v_i\eta)}, \tag{5}$$

where W_i is a radial windowing function, applied to suppress sidelobes that result from finite sampling of the frequency domain. From a wide choice of windowing functions, the Hamming window is used to keep our results comparable to TriHex:

$$W_i = 0.54 - 0.46\cos(2\pi\rho_i/\rho_{\max}). \tag{6}$$

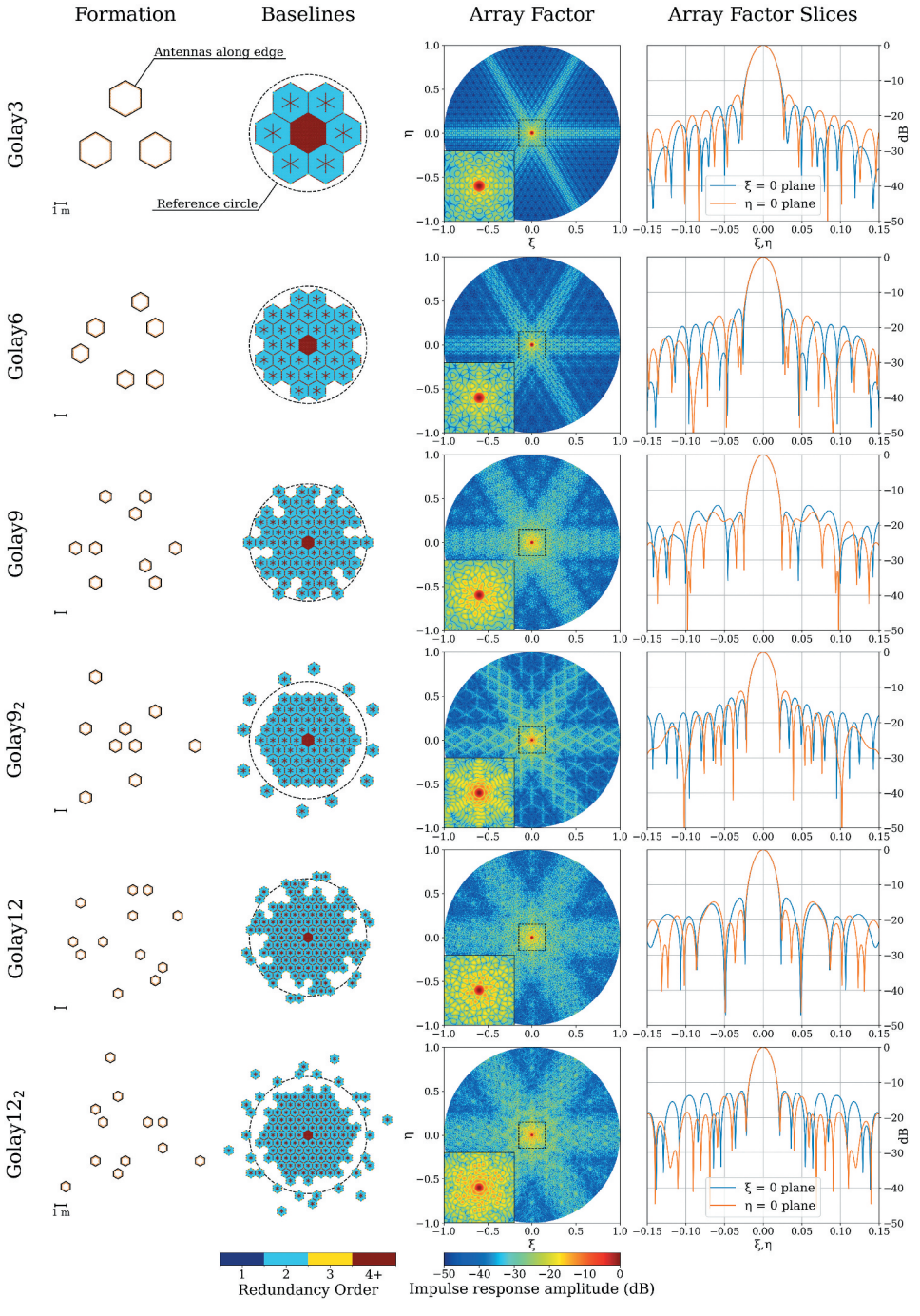

Figure 4. Performance of various Golay formations with 216 antennas in total. The baseline column includes a 40λ reference circle. The inset in the array factor column spans $-0.15 \leq \xi, \eta \leq 0.15$.

Table 1. Golay formation performance. *D* is the individual hexagon diameter.

D (m)	No. Sat.	Type	Max sidelobe(dB)	3 dB Beamwidth
3	3	Golay3	−14.2	1.55°
1.4	6	Golay6	−14.82	1.47°
0.9	9	Golay9	−14.39	1.36°
0.9	9	Golay9 $_2$	−11.11	1.29°
0.6	12	Golay12	−13.77	1.33°
0.6	12	Golay12 $_2$	−12.48	1.23°

The term $\rho_i = \sqrt{u_i^2 + v_i^2}$ is the radial distance of each baseline in the *uv* plane.

Table 1 summarizes the synthetic beam characteristics – specifically, the 3 dB (half-power) beamwidth and maximum sidelobe level – for the formations shown in Figure 4. We observe that formations with more satellites generally yield finer angular resolutions. This is attributed to fewer *uv* points having high (4+) redundancy. Instead, more antenna pairs form unique baselines, contributing to the performance. Two hundred and sixteen antennas arranged across six satellites (Golay6) will have 11% more unique baselines than if placed across three larger spacecraft (Golay3). Other Golay formations in Table 1 feature an even greater number of unique baselines, leading to improved angular resolution. However, this benefit is offset by gaps in *uv* coverage, which in turn increase sidelobe levels.

Furthermore, flying a larger number of smaller satellites has a key benefit of satellite redundancy. A malfunctioning satellite in a formation of three would remove more than half of the total *uv* coverage, with the remainder being arranged along a single spatial direction. An equivalent individual malfunction in a formation of six would remove less than a third of the total *uv* coverage and introduce gaps in *uv*. However, these can be partially mitigated by reorganising the formation for the new number of satellites. A larger number of satellites in a formation, however, come with additional complexity in formation keeping and operation.

Finally, it is worth emphasizing that Golay formations are agnostic to the physical size of the satellites. While this analysis scales satellite size to maintain a constant total antenna count for comparing different formations, Golay formations can also be applied without adjusting satellite size. For example, deploying six TriHex-sized satellites in a Golay6 formation – rather than three in Golay3 – would reduce the beamwidth from 1.55° to 0.735°, which would bring the spatial resolution at nadir from 15 km to 7 km, while also slightly improving sidelobe suppression. This flexibility makes Golay-based architectures attractive for future expandable or multi-phase missions.

6. HexSats

A notable recent advancement in nano-satellite technology is HexSats, a proposed flat, around 2.5 cm thick and roughly 1 m in diameter satellite platform well suited for high power and large aperture applications (Saddul et al. 2024). Designed for high-power and large-aperture applications, the structural mass of a HexSat is around 3 kg, with the capacity to deliver more than 200 W of power to its payload. In addition to low drag, the thin form of a HexSat allows them to stack well, and the hexagonal shape gives a superior packing efficiency in a circular rocket fairing when launching more than three stacks of satellites. As seen in Figures 1, 3 and 4, hexagonal antenna arrays also align naturally with this form factor, making HexSats a suitable option for interferometric missions.

HexSats are proposed to use many small thrusters that fit the thin form factor for orbit and formation keeping. These small thrusters produce thrust in micro-Newton levels and are distributed along the facesheets and the thickness of the satellite. In practice, the distributed micro-propulsion system (DμPS) would employ vacuum arc or electrospray thrusters to enable full 3-axis control, as illustrated in Figure 5.

Based on the results in Table 1, a Golay9 formation using HexSats could achieve an angular resolution of 1.36°, corresponding to a nadir spatial resolution of approximately 10 km at 420 km altitude. Due to their low-drag design, HexSats could also operate at altitudes as low as 250 km, improving the resolution to under 6 km.

HexSats have the potential to improve soil surface moisture and sea surface salinity data; however, several challenges remain. For one, precision flight of large formations has not yet been demonstrated. Proba-3 (launched in 2024) demonstrated sub-millimetre relative accuracy, but only for a two-spacecraft pair (European Space Agency 2025). Beyond holding a constant *uv* grid, tight control is required for collision avoidance. To relax these demands, General Circular Orbits (GCOs) can be employed (Vadali et al. 2008); they have been proposed for formations ranging from three satellites to swarms approaching a hundred spacecraft (Lützner et al. 2022; Martín-Neira et al. 2023). By reducing control effort, GCOs can also mitigate plume impingement and material deposition on neighbouring satellites.

Inter-satellite communication and correlation are likewise crucial. One approach, employed by TriHex, is to stream raw measurements between spacecraft via multiple laser links. An alternative (Lützner et al. 2022) time-stamps each antenna's data locally and forwards it to a single hub for correlation and processing, improving scalability but shifting the burden to inter-satellite timing and synchronisation.

Cross-satellite baseline calibration is equally critical. Single-satellite baselines can be calibrated via noise injection, as in SMOS (Brown et al. 2008), by distributing a common in-phase noise signal to multiple elements and compensating measured amplitude/phase errors. Inter-satellite baselines may be calibrated by pointing to Cold Sky (Martín-Neira et al. 2022) or by using microwave beacons at known locations to solve phase and baseline offsets (Sugihara El Maghraby et al. 2020); the beacon count can be reduced with a near-field beacon carried on a satellite within the formation's field of view.

Finally, the thin form factor of a HexSat is a major restriction, and it is not yet clear how all components and subsystems required for interferometric measurements will fit. HexSats will need to host stable time references for inter-satellite synchronization, high-rate laser or RF communication links, and onboard correlator units. Further research to solve these issues is ongoing.

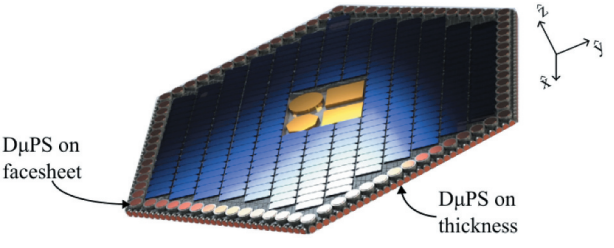

Figure 5. 'HexSat concept: a flat hexagonal satellite using the DμPS for orbital and attitude actuation' Saddul et al. (2024).

7. Conclusion

This work explored the application of Golay-based satellite formations for spaceborne passive microwave interferometry. For a given number of satellites, Golay formations offer the largest *uv* coverage by minimising redundancy in inter-satellite baselines. We have shown that distributing the same total number of antennas as in the TriHex mission concept (Golay3) across nine smaller satellites (Golay9) yields improved angular resolution of 1.36° and a lower maximum sidelobe level of −14.39 dB. In addition to performance gains, using a larger number of satellites enhances system robustness, as the impact of individual satellite failures is significantly reduced, at the cost of more complex formation keeping, cross-satellite calibration and operation. Finally, we demonstrated that implementing Golay formations on the HexSat nano-satellite platform can achieve L-band ground resolutions below 6 km.

Acknowledgements

The authors would like to thank the reviewer for their constructive comments, which helped substantially strengthen the practical context of this paper.

Disclosure statement

No potential conflict of interest was reported by the author(s).

References

Akins, A., A. Tanner, A. Colliander, N.-J. Schlegel, K. Boudad, I. Yanovsky, S. Brown, and S. Misra. 2025. "A Sparse Synthetic Aperture Radiometer Constellation Concept for Remote Sensing of Antarctic Ice Sheet Temperature." IEEE Transactions on Geoscience and Remote Sensing PP, 1–1. https://doi.org/10.1109/TGRS.2025.3534466

Beljaars, A., P. Viterbo, M. Miller, and A. Betts. 1996. "The Anomalous Rainfall Over the United States During July 1993: Sensitivity to Land Surface Parameterization and Soil Moisture Anomalies." *Monthly Weather Review* 124 (3): 362–383. https://doi.org/10.1175/1520-0493(1996)124<0362:TAROTU>2.0.CO;2

Berger, M., A. Camps, J. Font, Y. Kerr, J. Miller, J. Johannessen, B. Jacqueline, et al. 2002. "Measuring Ocean Salinity with ESA's SMOS Mission - Advancing the Science." *ESA Bulletin Bulletin ASE European Space Agency* 111.

Blackburn, S., A. Panoui, M. Paterson, and D. Stinson. 2009. "Honeycomb Arrays." *Electronic Journal of Combinatorics* 17 (1). https://doi.org/10.37236/444

Brown, M. A., F. Torres, I. Corbella, and A. Colliander. 2008. "SMOS Calibration." *IEEE Transactions on Geoscience and Remote Sensing* 46 (3): 646–658. https://doi.org/10.1109/TGRS.2007.914810

Camps, A., J. Bara, I. C. Sanahuja, and F. Torres. 1997. "The Processing of Hexagonally Sampled Signals with Standard Rectangular Techniques: Application to 2-D Large Aperture Synthesis Interferometric Radiometers." *IEEE Transactions on Geoscience and Remote Sensing* 35 (1): 183–190. https://doi.org/10.1109/36.551946

Camps, A., M. Vall-Llossera, I. Corbella, F. Torres, and N. Duffo. 2008. "Angular and Radiometric Resolution of Y-Shaped Nonuniform Synthetic Aperture Radiometers for Earth Observation." *IEEE Geoscience and Remote Sensing Letters* 5 (4): 793–795. https://doi.org/10.1109/LGRS.2008.2005915

Christensen, J., A. Carlstrom, H. Ekstrom, A. Emrich, J. Embretsen, P. de Maagt, and A. Colliander. 2007. "GAS: The Geostationary Atmospheric Sounder." In 2007 IEEE International Geoscience and Remote Sensing Symposium Barcelona, Spain ed. Tsang Leung, 223–226.

Condon, J. J., and S. M. Ransom. 2016. "Essential Radio Astronomy Spergel David N. ed." In *Chap*, 1–19. Vol. 1. Princeton University Press. , https://www.cv.nrao.edu/sransom/web/Ch1.html.

Corbella, I., N. Duffo, M. Vall-Llossera, A. Camps, and F. Torres. 2004. "The Visibility Function in Interferometric Aperture Synthesis Radiometry." *IEEE Transactions on Geoscience and Remote Sensing* 42 (8): 1677–1682. https://doi.org/10.1109/TGRS.2004.830641

Dirmeyer, P. A., and K. L. Brubaker. 1999. "Contrasting Evaporative Moisture Sources During the Drought of 1988 and the Flood of 1993." *Journal of Geophysical Research: Atmospheres* 104 (D16): 383–19,397. https://doi.org/10.1029/1999JD900222

Entekhabi, D., E. Njoku, P. O'Neill, K. H. Kellogg, W. Crow, W. N. Edelstein, J. Entin, et al. 2010. "The Soil Moisture Active and Passive (SMAP) Mission." Proceedings of the IEEE 98, 704–716. https://doi.org/10.1109/JPROC.2010.2043918

European Space Agency. 2024. "ESA – CIMR Facts and Figures." Last accessed October 10. https://www.esa.int/Applications/Observing_the_Earth/Copernicus/CIMR/CIMR_facts_and_figures

European Space Agency. 2025. "Proba-3 Becomes Two: Satellites Separated." Accessed October 10, 2025. https://www.esa.int/Enabling_Support/Space_Engineering_Technology/Proba-3/Proba-3_becomes_two_satellites_separated.

Gelzinis, M., and A. Wittig. 2025. *Non-Redundant HexSat Formations for Improved L-Band Data*. University of Southampton ePrints repository. https://eprints.soton.ac.uk/501139/1/Non-redundantHexSatformationsforimprovedL-banddata.pdf. Extended abstract.

Golay, M. J. E. 1971. "Point Arrays Having Compact, Nonredundant Autocorrelations." *Journal of the Optical Society of America* 61 (2): 272–273. https://doi.org/10.1364/JOSA.61.000272

Golomb, S. W., and H. Taylor. 1984. "Constructions and Properties of Costas Arrays." *Proceedings of the IEEE* 72 (9): 1143–1163. https://doi.org/10.1109/PROC.1984.12994

Goutoule, J.-M., and F. De Boer. 2000. "Large Interferometer Antennas Synthesised by Satellites in Formation for Earth Remote Sensing." In *IGARSS 2000 – 2000 IEEE International Geoscience and Remote Sensing Symposium. Proceedings (Cat. No. 00CH37120)*, edited by Tammy I. Stein, 869–870, Vol. 2, Honolulu, HI, USA.

Jiménez, C., J. Tenerelli, C. Prigent, L. Kilic, T. Lavergne, S. Skarpalezos, J. L. Høyer, N. Reul, and C. Donlon. 2021. "Ocean and Sea Ice Retrievals from an End-To-End Simulation of the Copernicus Imaging Microwave Radiometer (CIMR) 1.4–36.5 GHz Measurements." *Journal of Geophysical Research: Oceans* 126 (12). 10.1029/2021JC017610.

Johnson, J. T., K. C. Jezek, G. Macelloni, M. Brogioni, L. Tsang, E. P. Dinnat, J. P. Walker, et al. 2021. "Microwave Radiometry at Frequencies from 500 to 1400 MHz: An Emerging Technology for Earth Observations." *IEEE Journal of Selected Topics in Applied Earth Observations and Remote Sensing* 14:4894–4914. https://doi.org/10.1109/JSTARS.2021.3073286

Kerr, Y. H., D. De Castro, A. Zurita, and J. Closa. 2019. *Low Frequency Passive Microwave User Requirement Consolidation Study: Cluster Analysis Report*. Technical Report SO-TN-CB-GS-0082. CESBIO. https://hal.science/hal-04845270.

Kerr, Y. H., N. Rodriguez-Fernandez, E. Anterrieu, M.-J. Escorihuela, M. Drusch, J. Closa, A. Zurita, et al. 2020. "The Next Generation of L Band Radiometry: User's Requirements and Technical Solutions." In *IGARSS 2020 – 2020 IEEE International Geoscience and Remote Sensing Symposium*, edited by Bill Emery, 5974–5977. Waikoloa, HI, USA.

Kerr, Y. H., P. Waldteufel, J.-P. Wigneron, J. Martinuzzi, J. Font, and M. Berger. 2001. "Soil Moisture Retrieval from Space: The Soil Moisture and Ocean Salinity (SMOS) Mission." *IEEE Transactions on Geoscience and Remote Sensing* 39 (8): 1729–1735. https://doi.org/10.1109/36.942551

Lang, R., Y. Zhou, C. Utku, and D. Le Vine. 2016. "Accurate Measurements of the Dielectric Constant of Seawater at L Band." *Radio Science* 51 (1): 2–24. https://doi.org/10.1002/2015RS005776

Le Vine, D. M., A. J. Griffis, C. T. Swift, and T. J. Jackson. 1994. "ESTAR: A Synthetic Aperture Microwave Radiometer for Remote Sensing Applications." *Proceedings of the IEEE* 82 (12): 1787–1801. https://doi.org/10.1109/5.338071

Lukas, R., and E. Lindstrom. 1991. "The Mixed Layer of the Western Equatorial Pacific Ocean." *Journal of Geophysical Research* 96 (S01): 3343–3358. https://doi.org/10.1029/90JC01951

Lützner, M., T. Jagdhuber, A. Camps, H. Park, M. Peichl, R. Förstner, and M. Jirousek. 2022. "Orbit Design for a Satellite Swarm-Based Motion Induced Synthetic Aperture Radiometer (MISAR) in

Low-Earth Orbit for Earth Observation Applications." *IEEE Transactions on Geoscience and Remote Sensing* 60:1–16. https://doi.org/10.1109/TGRS.2022.3152898

Martín-Neira, M., M. Piera, F. Scala, C. Colombo, A. Zurita, and B. Duesmann. 2022. "Formation Flying L-band Aperture Synthesis Mission Concept." In *IGARSS 2022 – 2022 IEEE International Geoscience and Remote Sensing Symposium*, edited by Hean Teik Chuah, 7325–7328. Kuala Lumpur, Malaysia.

Martín-Neira, M., F. Scala, A. M. Zurita, M. Suess, M. Piera, B. J. Duesmann, M. Drusch, et al. 2023. "TriHex: Combining Formation Flying, General Circular Orbits, and Alias-Free Imaging, for High-Resolution L-Band Aperture Synthesis." *IEEE Transactions on Geoscience and Remote Sensing* 61:1–17. https://doi.org/10.1109/TGRS.2023.3268560

McKay, D., T. Grydeland, and B. Gustavsson. 2022. "Manx Arrays: Perfect Non-redundant Interferometric Geometries." *Radio Science* 57 (9): 1–8. https://doi.org/10.1029/2022RS007500

Moreno-Galbis, P., J. Kainulainen, and M. Martin-Neira. 2007. "Experimental Demonstration of the Corbella Equation for Aperture Synthesis Microwave Radiometry." *IEEE Transactions on Geoscience and Remote Sensing* 45 (4): 945–957. https://doi.org/10.1109/TGRS.2006.888863

Nairizi, S., and J. R. Rydzewski. 1977. "Effects of Dated Soil Moisture Stress on Crop Yields." *Experimental Agriculture* 13 (1): 51–59. https://doi.org/10.1017/S0014479700007602

Ruf, C. S., C. T. Swift, A. B. Tanner, and D. M. Le Vine. 1988. "Interferometric Synthetic Aperture Microwave Radiometry for the Remote Sensing of the Earth." *IEEE Transactions on Geoscience and Remote Sensing* 26 (5): 597–611. https://doi.org/10.1109/36.7685

Saddul, K., J. Saletes, M. Kim, and A. Wittig. 2024. "HexSats: A Novel Flat Hexagonal Nanosatellite for High-Power Applications." *Acta Astronautica* 225:27–40. https://doi.org/10.1016/j.actaastro.2024.09.007

Schmugge, T. J. 1980. "Effect of Texture on Microwave Emission from Soils." *IEEE Transactions on Geoscience and Remote Sensing* GE-18 (4): 353–361. https://doi.org/10.1109/TGRS.1980.350313

Sharp, E. 1961. "A Triangular Arrangement of Planar-Array Elements That Reduces the Number Needed." *IRE Transactions on Antennas and Propagation* 9 (2): 126–129. https://doi.org/10.1109/TAP.1961.1144967

Sugihara El Maghraby, A. K., A. Grubišić, C. Colombo, and A. Tatnall. 2018. "A Novel Interferometric Microwave Radiometer Concept Using Satellite Formation Flight for Geostationary Atmospheric Sounding." *IEEE Transactions on Geoscience and Remote Sensing* 56 (6): 3487–3498. https://doi.org/10.1109/TGRS.2018.2800534

Sugihara El Maghraby, A. K., H. Park, A. Camps, A. Grubišić, C. Colombo, and A. Tatnall. 2020. "Phase and Baseline Calibration for Microwave Interferometric Radiometers Using Beacons." *IEEE Transactions on Geoscience and Remote Sensing* 58 (8): 5242–5253. https://doi.org/10.1109/TGRS.2019.2949891

Ulaby, F. T., R. K. Moore, and A. K. Fung. 1981. *Microwave Remote Sensing. Active and Passive. Volume 1. Microwave Remote Sensing Fundamentals and Radiometry*. Artech House.

Vadali, S. R., P. Sengupta, H. Yan, and K. T. Alfriend. 2008. "Fundamental Frequencies of Satellite Relative Motion and Control of Formations." *Journal of Guidance, Control, and Dynamics* 31 (5): 1239–1248. https://doi.org/10.2514/1.34790

Zurita, A. M., I. Corbella, M. Martín-Neira, M. A. Plaza, F. Torres, and F. J. Benito. 2013. "Towards a SMOS Operational Mission: SMOSOps-Hexagonal." *IEEE Journal of Selected Topics in Applied Earth Observations and Remote Sensing* 6 (3): 1769–1780. https://doi.org/10.1109/JSTARS.2013.2265600